






Article

Obtaining of ZnO/Fe₂O₃ Thin Nanostructured Films by AACVD for Detection of ppb-Concentrations of NO₂ as a Biomarker of Lung Infections

Artem S. Mokrushin ^{1,*}, Yulia M. Gorban ^{1,2}, Aleksey A. Averin ³, Philipp Yu. Gorobtsov ¹, Nikolay P. Simonenko ¹, Yury Yu. Lebedinskii ⁴, Elizaveta P. Simonenko ¹ and Nikolay T. Kuznetsov ¹

¹ Kurnakov Institute of General and Inorganic Chemistry of the Russian Academy of Sciences, Moscow 119991, Russia; julia_gorban@bk.ru (Y.M.G.); phigoros@gmail.com (P.Y.G.); n_simonenko@mail.ru (N.P.S.); ep_simonenko@mail.ru (E.P.S.); ntkuz@igic.ras.ru (N.T.K.)

² Faculty of Technology of Inorganic Substances and High Temperature Materials, Mendeleev University of Chemical Technology of Russia, Moscow 125047, Russia

³ Frumkin Institute of Physical Chemistry and Electrochemistry, Russian Academy of Sciences, Moscow 199071, Russia; alx.av@yandex.ru

⁴ Moscow Institute of Physics and Technology, Dolgoprudny 141700, Russia; yylebedinskij@mephi.ru

* Correspondence: artyom.nano@gmail.com

Abstract: ZnO/Fe₂O₃ nanocomposites with different concentration and thickness of the Fe₂O₃ layer were obtained by two-stage aerosol vapor deposition (AACVD). It was shown that the ZnO particles have a wurtzite structure with an average size of 51–66 nm, and the iron oxide particles on the ZnO surface have a hematite structure and an average size of 23–28 nm. According to EDX data, the iron content in the films was found to be 1.3–5.8 at.%. The optical properties of the obtained films were studied, and the optical band gap was found to be 3.16–3.26 eV. Gas-sensitive properties at 150–300 °C were studied using a wide group of analyte gases: CO, NH₃, H₂, CH₄, C₆H₆, ethanol, acetone, and NO₂. A high response to 100 ppm acetone and ethanol at 225–300 °C and a high and selective response to 300–2000 ppb NO₂ at 175 °C were established. The effect of humidity on the magnitude and shape of the signal obtained upon NO₂ detection was studied.

Keywords: AACVD; chemoresistive gas sensors; zinc oxide (ZnO); iron oxide (Fe₂O₃); thin films; nanocomposites; nitrogen dioxide (NO₂); two-dimensional nanomaterials



Citation: Mokrushin, A.S.; Gorban, Y.M.; Averin, A.A.; Gorobtsov, P.Y.; Simonenko, N.P.; Lebedinskii, Y.Y.; Simonenko, E.P.; Kuznetsov, N.T. Obtaining of ZnO/Fe₂O₃ Thin Nanostructured Films by AACVD for Detection of ppb-Concentrations of NO₂ as a Biomarker of Lung Infections. *Biosensors* **2023**, *13*, 445. <https://doi.org/10.3390/bios13040445>

Received: 24 February 2023

Revised: 26 March 2023

Accepted: 29 March 2023

Published: 31 March 2023



Copyright: © 2023 by the authors. Licensee MDPI, Basel, Switzerland. This article is an open access article distributed under the terms and conditions of the Creative Commons Attribution (CC BY) license (<https://creativecommons.org/licenses/by/4.0/>).

1. Introduction

Semiconductor gas sensors based on metal oxides (MOS sensors) are widely used to detect toxic and explosive gases in air [1]. Devices with gas sensors of this type have a relatively low cost, high speed, high accuracy, high miniaturization potential, and are easy to operate [2].

Zinc oxide (*n*-type semiconductor with $E_g = 3.37$ eV) is one of the most widely used gas-sensitive materials in MOS sensors [3]. ZnO thin films exhibit good electrical conductivity, chemical stability, high ultraviolet (UV) absorption, and low toxicity [4,5]. Despite the unique physical and chemical properties, individual ZnO in the composition of chemoresistive gas sensors has some drawbacks: limited maximum sensitivity, low selectivity, high operating temperature, and long response and recovery times [6].

Various approaches to ZnO modification are used to improve its gas sensing properties. Increase in sensitivity can be achieved by using various transition metals (Fe, Cu, Ni, Y, etc.) as dopants [7–10]. Doping with lanthanides (Ce, Er) can not only improve the sensor response, but it also reduces the operating temperature [11,12]. Decoration with noble metals (Pd, Pt, Au, etc.) allows a significant increase in the response and selectivity to certain gases due to chemical and electronic sensitization [13–16]. Creating nanocomposites with other metal oxides (SnO₂, CuO, NiO, etc.) is also an effective method to improve

gas-sensitive properties by forming *p-n* or *n-n* heterojunctions and changing the thickness of the electron-depleted layer [17–20]. A suitable material for the synthesis of composites with a *n-n* heterojunction is α -Fe₂O₃ (a *n*-type semiconductor with a bandgap of 2.2 eV), which is readily accessible and relatively cheap [21,22].

A wide variety of synthetic techniques and approaches are used to produce ZnO/ α -Fe₂O₃ nanocomposites. Thus, in [1] ZnO, nanorods were produced by chemical solution deposition (CSD) and then doped with α -Fe₂O₃ using liquid-phase ion layering (SILAR). This approach increased the response to ethanol (400 ppm) from 15.5 at 300 °C to 39 at 240 °C. In [23], zinc oxide was obtained by thermal evaporation followed by solvothermal precipitation of α -Fe₂O₃. The film had a seven-fold higher response to 2000 ppm ethanol compared to individual ZnO. In [24], the ZnO/ α -Fe₂O₃ nanocomposite was obtained by solvothermal method. This material exhibited an increase in response to 100 ppm acetone from 7.2 to 29.9 at 290 °C, as well as a decrease in detection time compared to individual iron oxide. ZnO particles in the shape of three-dimensional tetrapods, doped with Fe₂O₃ nanoparticles, was obtained by flame transport synthesis, followed by addition of iron microparticles and annealing. The addition of Fe₂O₃ allowed us to achieve a high response to 100 ppm ethanol at room temperature and reduced the dependence of sensing properties on humidity [25]. In work [26], ZnO nanofilaments were obtained by the vapor–liquid–solid process, and then the precursor solution for α -Fe₂O₃ was deposited on ZnO by spin-coating, with resulting sample further annealed in a nitrogen atmosphere. At the Fe₂O₃ concentration of 0.05 M, the highest response value (18.8) to 100 ppm CO at 300 °C was achieved.

Compared to other synthesis techniques, aerosol-assisted chemical vapor deposition (AACVD) is a convenient way to produce thin nanostructured films of a given chemical composition with different morphologies. This method possesses a simple hardware design, low cost, and availability of precursors [27–29]. It is based on the atomization of a liquid precursor solution into aerosol droplets, which are subsequently transported to the heated reaction zone, where the solvent undergoes rapid evaporation and/or decomposition, forming a film of a given chemical composition on the substrate surface [30]. The literature contains data on the formation of ZnO/Fe₂O₃ nanocomposite with developed morphology by two-stage AACVD [31]. ZnCl₂ solution in ethanol was used as a precursor to obtain ZnO particles at a synthesis temperature of 450 °C, then, at the same temperature, Fe₂O₃ was deposited on the obtained ZnO particles using acetone solution of FeCl₃·6H₂O. This approach made it possible to obtain spear-shaped ZnO rods with a height of 1.2 μ m and a diameter of 80 nm with flake-shaped Fe₂O₃ particles deposited on them. The total thickness of these structures formed on ZnO rods is about 200 nm.

Currently, gas sensors based on metal oxides are widely used not only in the environmental, automotive, and chemical industries for the detection of various gases, but they are also used in medicine. Methods of noninvasive diagnostics and patient monitoring based on the analysis of exhaled air using chemoresistive gas sensors are a modern alternative to more complex analytical methods, such as chromatography, mass spectrometry, etc. Such devices, based on MOS-gas sensors, are portable and easy to use, as well as allowing to diagnose diseases at an early stage [32]. Nevertheless, various studies are ongoing to develop the topology of such devices, as well as the search for new gas-sensitive materials capable of detecting gases that are biomarkers of various diseases [33,34]. Such disease biomarkers can be volatile organic compounds (VOC)—ethanol, acetone, toluene, as well as inorganic compounds (NO_x, H₂S, NH₃) [35]. For example, increased concentrations of NO_x in exhaled air have been reported in patients with inflammatory lung diseases, such as bronchial asthma, bronchiectasis, and chronic obstructive pulmonary disease (COPD) [32,36,37]. The use of gas sensors in medicine requires the registration of analyte gases (NO₂, ethanol, acetone, toluene, H₂S, and others) at concentrations of less than 100 ppb, which is significantly below the lower detection limits for environmental monitoring (about tens and hundreds ppm) [38,39]. Thus, gas sensors used for medical

purposes must be highly sensitive to ultra-low gas concentrations, selective, and have minimal dependence on humidity.

We found no data on the use of the AACVD process to produce ZnO/Fe₂O₃ nanocomposites for chemical gas sensing, so the aim of this work was to obtain thin nanostructured ZnO/Fe₂O₃ films by the AACVD method for chemoresistive gas sensors, as well as to study the influence of the Fe₂O₃ amount on the gas-sensitive properties, including the detection of NO₂, a biomarker of various diseases.

2. Materials and Methods

2.1. AACVD Synthesis of ZnO/Fe₂O₃ Films

An amount of 0.05 M solutions of zinc acetylacetonate [Zn(H₂O)(O₂C₅H₇)₂] and iron acetylacetonate [Fe(O₂C₅H₇)₃] in methanol CH₃OH (>99%, Chimmed) were used in the AACVD synthesis. Zinc and iron acetylacetonates were synthesized using zinc nitrate Zn(NO₃)₂·6H₂O (>98%, “Reachem”), iron chloride, FeCl₃·6H₂O (>98%, “Reachem”), and acetylacetonone (>98%, “Ecos-1”) by neutralization of their solutions with 5% ammonia hydrate solution (NH₃·H₂O, >99%, “Ecos-1”). ZnO films were obtained using a special laboratory setup consisting of a gas flow meter, an ultrasonic generator (Albedo IN-7), a furnace with a flow chamber, and an aerosol trapping system. To maintain constant conditions of aerosol formation, flow-through water cooling of the ultrasonic generator was performed. Aerosol deposition was performed in a flow furnace chamber on various substrates (glass, aluminum oxide, and an Al₂O₃ sensor with platinum counter-pin electrodes and a microheater on the reverse side [40]) at a decomposition temperature of 400 °C. Nitrogen (high purity grade “6.0”) was used as a carrier gas, with a flow rate of 300 mL/min. At the first stage, using zinc acetylacetonate solution, ZnO film was obtained (sample Z) with a deposition time of 60 min. In the second step, a Fe₂O₃ film was deposited on the surface of the ZnO film using iron acetylacetonate solution for 10, 20, and 30 min at 400 °C, which are called Z1Fe, Z2Fe, and Z3Fe, respectively, in the further text. For additional analysis by Raman spectroscopy, a film of individual Fe₂O₃ was synthesized on an Al₂O₃ substrate under the following conditions: sputtering time of 45 min at 400 °C. The scheme of the laboratory setup used for AACVD synthesis of ZnO/Fe₂O₃ thin nanostructured films used in this work is shown in Figure 1. After synthesis, additional heat treatment of the coatings was performed at 350 °C for 2 h in the air for additional removal of organic compounds from the surface of the films.

Scheme of the setup for AACVD synthesis

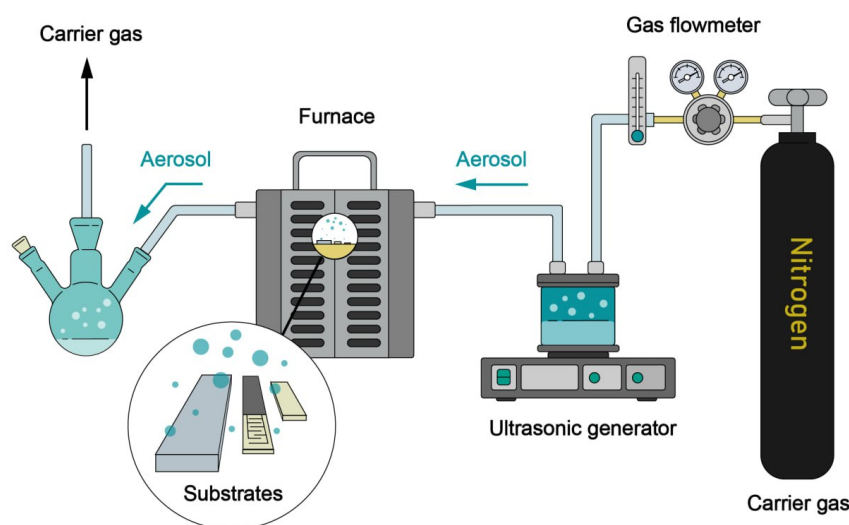


Figure 1. Scheme of the setup for AACVD synthesis of ZnO/Fe₂O₃ thin films.

2.2. Instrumentation

XRD patterns of the coatings on glass substrates were recorded on a D8 Advance X-ray diffractometer (Bruker) with $\text{CuK}\alpha$ emission in the range of 2θ 25° – 65° in 0.02° increments with signal accumulation at the point for 1.8 s. The morphology and microstructure of the films on Al_2O_3 substrates were studied using a NVision 40 three-beam workstation (Carl Zeiss). Electronic UV transmission spectra of $\text{ZnO}/\text{Fe}_2\text{O}_3$ films on glass substrates were recorded using a SF-56 UV-Vis spectrophotometer. Raman spectra were obtained with a Renishaw inVia Reflex spectrometer using a 405 nm diode laser as the excitation source. All spectra were recorded in the 100 – 2000 cm^{-1} range with a spectral resolution of ~ 3 cm^{-1} through a $50\times$ (NA 0.5, FN 26.5) magnification lens, with an irradiated site diameter of ~ 2 μm . The incident radiation power was less than 2.5 mW. Grating: 2400, and the signal accumulation time was 300 s.

The gas-sensitive properties were measured on a specialized precision setup [41–43]. The gas environment in the quartz cell was created using four Bronkhorst gas flow controllers with maximum flow rates of 1, 50, 100, and 200 mL/min. The temperature of the sensor element was regulated using a built-in platinum microheater pre-calibrated using a Testo 868 thermal imager. The resulting film was studied for sensitivity to the following analyte gases: CO , H_2 , CH_4 , NH_3 , benzene, acetone, ethanol, and NO_2 . The corresponding test gas mixtures in air were used as a source of the analyzed gases, and synthetic air was used to construct a baseline. To measure the signal at different relative humidity (RH), we used a special unit with a bubbler, and the RH of the gas mixture was controlled by a digital flow-through hygrometer «Excis». Electrical resistance of oxide films was measured using a Fluke 8846A (6.5 Digit Precision Multimeter) with an upper limit of 1 GOhm. The response to CO , H_2 , CH_4 , NH_3 , benzene, acetone, and ethanol was calculated using the formula:

$$S = R_{\text{Air}}/R, \quad (1)$$

where R_{Air} is the resistance of the oxide film in the synthetic air medium; R —in the environment with a given concentration of the analyte gas. The response to NO_2 was calculated by the inverse relation (1).

The selectivity coefficient was calculated by the following equation:

$$\text{Sel} = S_{\text{NO}_2}/S_2, \quad (2)$$

where S_{NO_2} is the response when detecting 2 ppm NO_2 ; S_2 is the response to a given gas concentration (in our case it was 100 ppm ethanol or acetone), to which the highest response value after NO_2 was observed.

The following ratio was used to calculate «response drop» (RD) in a humid atmosphere $RD = \frac{R_0 - R_{RH}}{R_0} \times 100\%$, where R_0 is the response at 0% RH, R_{RH} is the response at the corresponding RH.

3. Results and Discussion

3.1. Chemical and Phase Composition

The chemical composition of the obtained $\text{ZnO}/\text{Fe}_2\text{O}_3$ films was studied by energy dispersive X-ray spectroscopy (EDX). The EDX mapping of zinc and iron shows (Figure 2) that both metals are evenly distributed on the surface of the obtained films. The calculated EDX values showed that the iron content in Z1Fe, Z2Fe and Z3Fe films was 1.3, 4.8 and 5.8 at.%, respectively. Thus, when the sputtering time of the Fe_2O_3 film increases from 10 to 30 min, the iron content of the $\text{ZnO}/\text{Fe}_2\text{O}_3$ nanocomposite films increases proportionally.

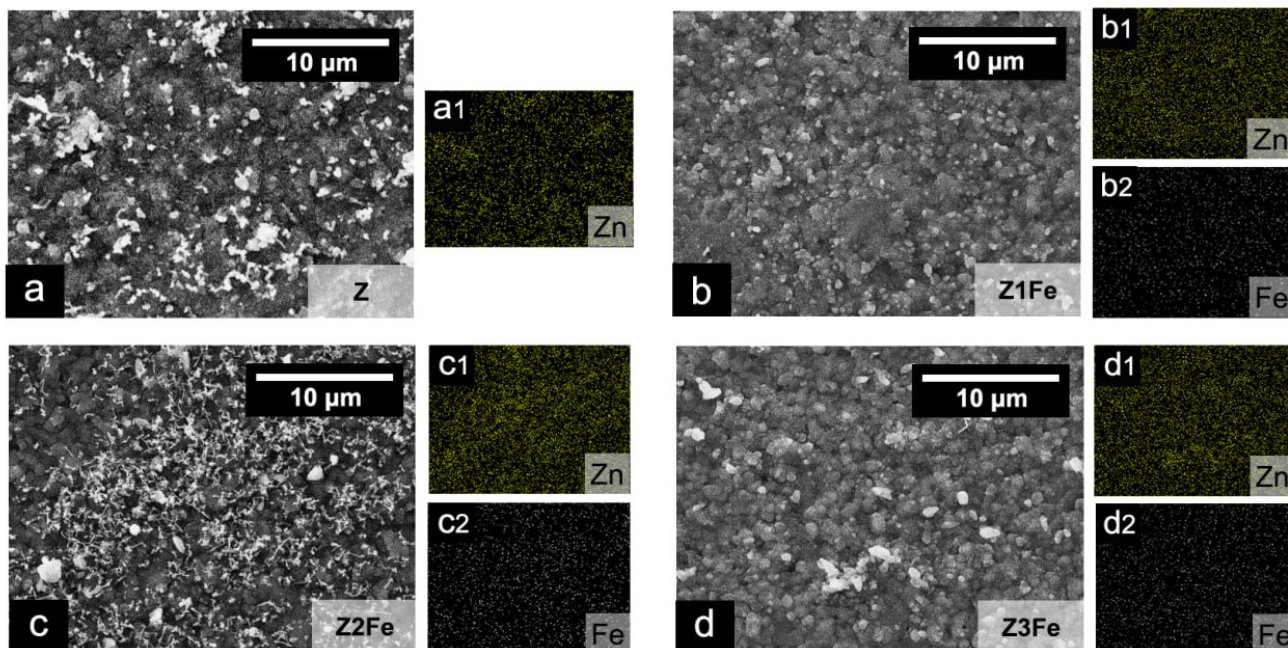


Figure 2. EDX mapping of zinc and iron in thin films of ZnO/Fe₂O₃: (a) Z, (b) Z1Fe, (c) Z2Fe, and (d) Z3Fe with Zn and Fe element distribution (a1–d2).

Due to the small thickness of the synthesized films, the diffractograms obtained for films on polycrystalline Al₂O₃ substrates are uninformative. Against the background of intense substrate reflexes, low-intensity film reflexes are practically indiscernible. Therefore, X-ray phase analysis of ZnO/Fe₂O₃ thin films was performed on X-ray amorphous glass substrates. According to the data of X-ray phase analysis (Figure 3a) of ZnO/Fe₂O₃ thin films on glass substrates it was found that, for all samples, the presence of characteristic reflexes of hexagonal ZnO wurtzite phase (spatial group P63mc, PDF 01-070-8070) is observed [44]. The most intense reflex (002) is observed at 34.4° 2θ, which indicates a strong preferential orientation in the [001] direction. Crystallite growth variations are related to solvent polarity, so the intensity of reflex (002) may be due to the use of methanol, which has one of the highest polarities of all organic solvents, in the AACVD process [30]. The mean sizes of ZnO crystallites calculated by the Scherrer formula for samples Z, Z1Fe, Z2Fe, and Z3Fe were 40, 42, 30, and 35 nm, respectively. No separate iron-containing phases were detected on the diffractograms, which may be due to the low concentration of iron oxide, the small thickness of the Fe₂O₃ layer, and the instrumental feature of the diffractometer in which the copper tube was installed. It is also worth noting that, for samples Z1Fe, Z2Fe, and Z3Fe, no shift in reflexes relative to individual ZnO is observed, which is an indirect sign of the formation of a two-phase nanocomposite rather than a solid solution.

Additionally, synthesized ZnO/Fe₂O₃ thin films on Al₂O₃ substrates were studied by Raman spectroscopy. As can be seen from Figure 3b, besides the peaks related to the α-Al₂O₃ substrate (A_{1g} at 418 and 644 cm⁻¹ and E_g at 378, 430, 450, 576 and 749 cm⁻¹) [45], an intense ZnO peak at 577 cm⁻¹, corresponding to A₁(LO) mode, is observed in all samples. In addition, peaks assigned to the (E₂^{high}–E₂^{low}), E₂^{high}, 2TO, and [2A₁(LO), E₁(LO), 2LO] modes were observed at 332, 438, 982, and 1153 cm⁻¹, respectively [46]. Two peaks at 1356 and 1607 cm⁻¹ can be attributed to the D- and G-bands of residual carbon that remained after the synthesis. Figure 3c shows the spectrum of the individual iron oxide film. As can be seen, besides the α-Al₂O₃ substrate peaks, bands at 226, 501 (A_{1g}) and 296 (E_g) cm⁻¹ with low intensity, characteristic of α-Fe₂O₃ (trigonal syngony, hematite phase, space group R3c), are observed [47]. Figure 3d shows that the α-Fe₂O₃ peaks at 226 and 296 cm⁻¹ in the spectra of Z1Fe, Z2Fe, and Z3Fe samples are also low in

intensity. The weak signal from α -Fe₂O₃ may indicate the low concentration and thickness of the iron oxide layer. Slightly more intense peaks are observed for the Z3Fe sample due to the higher concentration of iron oxide. The obtained peaks related to Fe₂O₃, although low-intensity, allow us to establish the formation of the ZnO/ α -Fe₂O₃ nanocomposite.

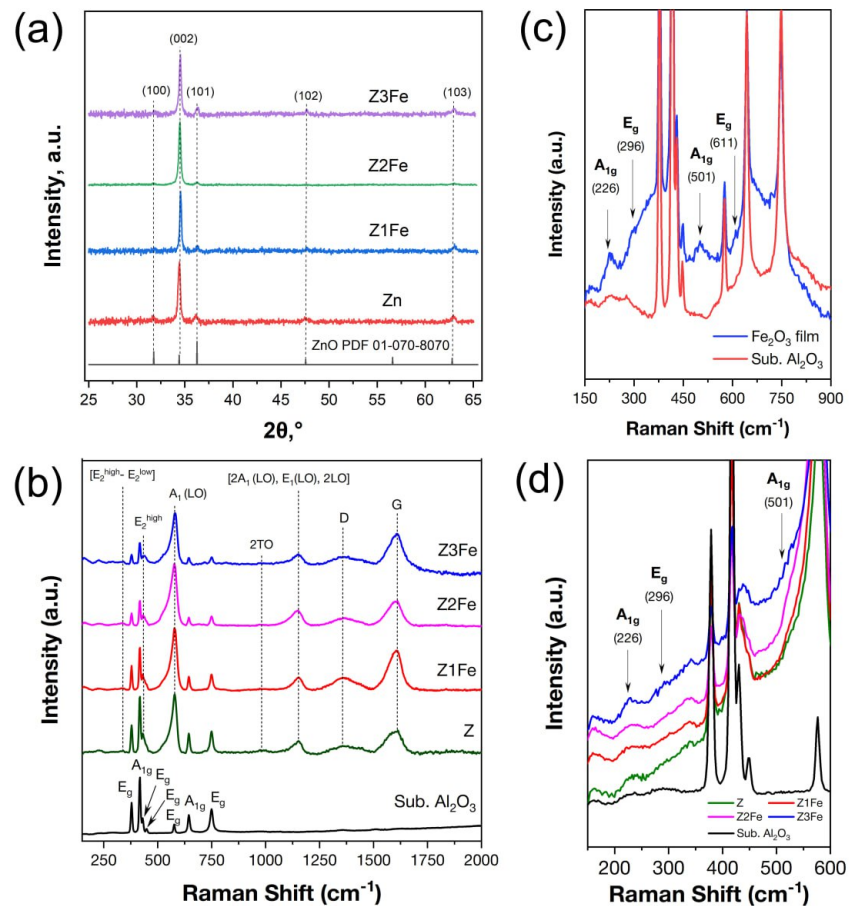


Figure 3. XRD-pattern for ZnO/Fe₂O₃ films on glass substrate (a) and Raman spectra for ZnO/Fe₂O₃ thin films on Al₂O₃ (b); enlarged Raman spectra of individual Fe₂O₃ (c) and ZnO/Fe₂O₃ films on Al₂O₃ substrate (d).

Figure 4a shows an overview XPS spectrum of Z and Z3Fe samples. As can be seen, the spectrum contains signals of the element peaks: Zn, O, and C (for the sample ZnO), as well as weakly intense signals from Fe (for the sample Z3Fe). It is likely that carbon is in the composition of CO₂ sorbed on the surface of the materials, as well as residual products after the synthesis. Figure 4b shows the XPS spectra of Zn 2p. Two peaks of Zn 2p_{1/2} and Zn 2p_{3/2} can be seen on the plot: at 1045.4 and 1022.3 eV, 1045.2 and 1022.1 eV for ZnO, and Z3Fe samples, respectively. The spin-orbit splitting was 23.1 eV, which is typical for ZnO with the wurtzite structure and agrees well with the literature data [48,49].

Figure 4c shows the XPS spectra of the Fe 2p sample Z3Fe. Two pronounced peaks of Fe 2p_{1/2} and Fe 2p_{3/2} at 723.5 and 710.3 eV can be seen on the plot. The signals obtained can equally be attributed to both Fe₂O₃ and Fe₃O₄ [50]. The main difference between Fe₂O₃ and Fe₃O₄ on the XPS spectra is the presence of a satellite peak for Fe₂O₃ between Fe 2p_{1/2} and Fe 2p_{3/2} [51,52], which was also observed in our case at 717.5 eV. Therefore, based on the XPS data obtained, we can assert the formation of the Fe₂O₃ phase within the thin films, which agrees well with the Raman spectroscopy data.

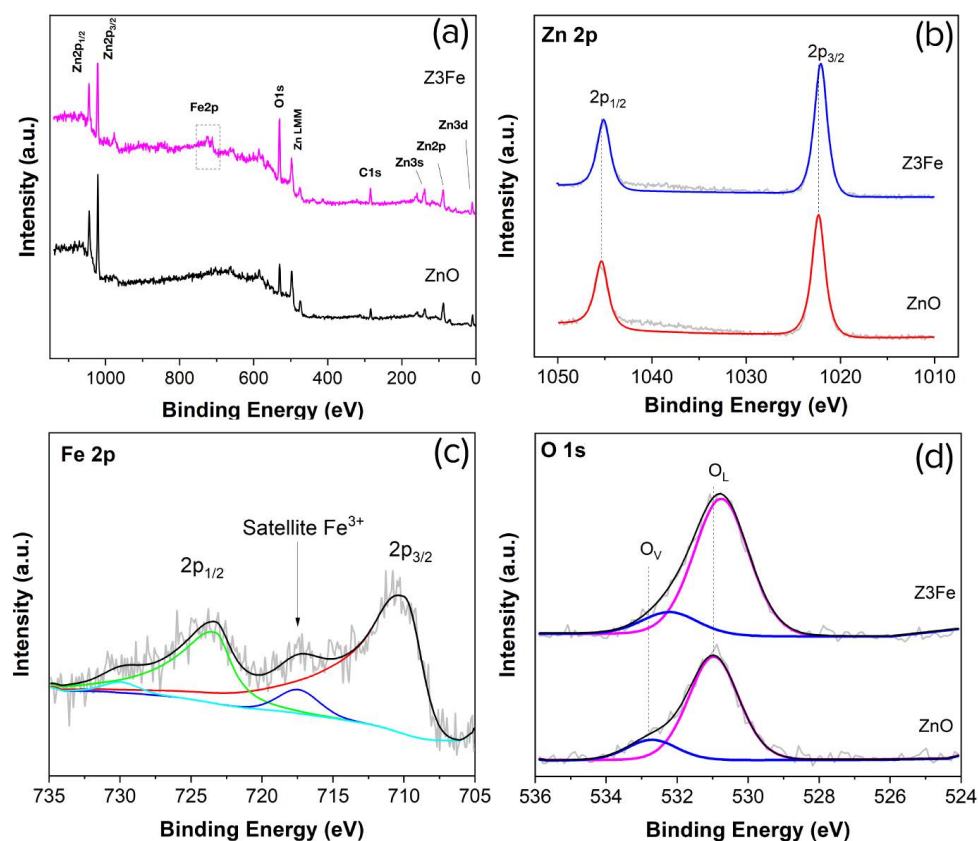


Figure 4. XPS spectra of ZnO and Z3Fe thin films: overview (a), Zn 2p (b), Fe 2p (c), and O 1s (d); on the spectra (c,d), coloured lines indicate the different components.

Figure 4d shows the O 1s spectra. As can be seen, 2 O_L and O_V peaks are present in the spectra: at 531.0 and 532.8 eV, as well as 530.8 and 532.3 eV, for ZnO and Z3Fe samples, respectively. The O_L peak refers to the lattice oxygen (O^{2-}) in the crystal structure of ZnO and Fe_2O_3 , while the O_V signal probably refers to oxygen vacancies and/or oxygen-containing groups (e.g., O^-) sorbed on the surface [53,54]. When Fe_2O_3 is modified, the maxima of the main peaks of all elements are shifted by 0.2–0.5 eV, which may be related to the effect of the modifying additive and the formation of the Schottky barrier in the nanocomposite.

3.2. Microstructure and Morphology

The microstructure and dispersity of ZnO/ Fe_2O_3 thin films on Al_2O_3 substrates were studied by scanning electron microscopy (SEM). As can be seen (Figure 5), all films uniformly cover the substrate surface, forming a continuous coating. The lower layer of ZnO in all films consists of spherical nanoparticles. In sample Z, the size of ZnO nanoparticles is 66 ± 13 nm, Z1Fe: 50 ± 14 nm, and Z2Fe: 51 ± 10 nm, and, in Z3Fe, the iron oxide covers the ZnO particles tightly, due to which it is not possible to calculate their size. The data obtained correlate well with the calculated crystallite values estimated using the Scherrer method on the obtained X-ray diffraction patterns. Z2Fe and Z3Fe samples show Fe_2O_3 nanoparticles on the ZnO surface, their size in the Z2Fe sample being 23 ± 4 nm, and, with increasing sputtering time (Z3Fe), their size increases to 28 ± 5 nm. Due to the low concentration of iron in the Z1Fe sample, it is not possible to estimate the size of Fe_2O_3 nanoparticles.

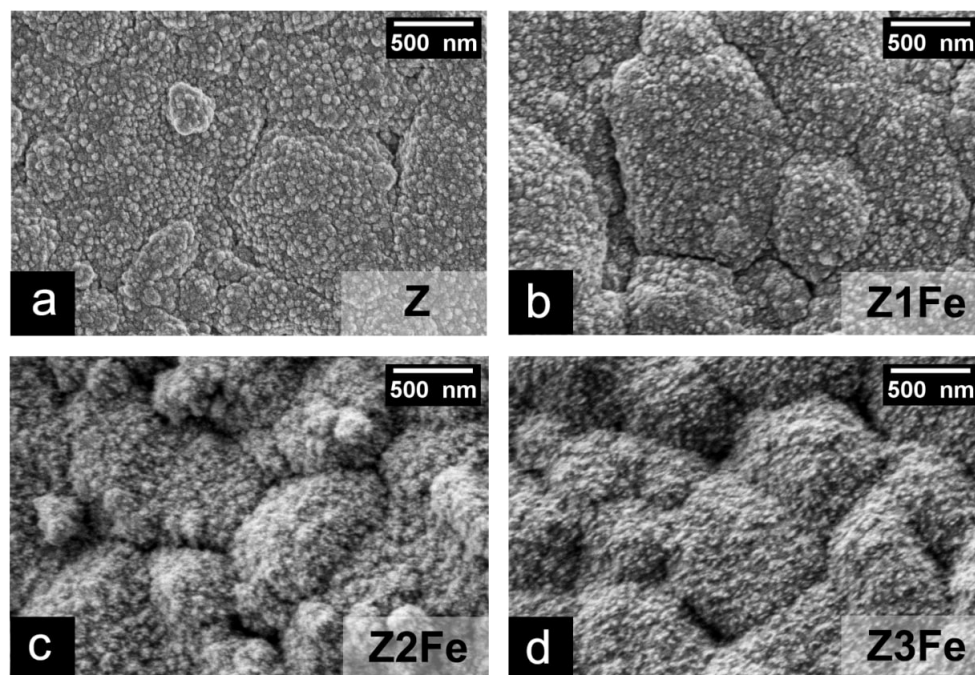


Figure 5. SEM micrographs for thin films of ZnO/Fe₂O₃: Z (a), Z1Fe (b), Z2Fe (c), and Z3Fe (d).

Figure 6 shows microphotographs of chips of glass substrates with Z(a) and Z3Fe (b) films applied. The calculated film thickness values for Z, Z1Fe, Z2FE, and Z3Fe were 174 ± 29 , 181 ± 11 , 185 ± 40 , and 198 ± 30 nm, respectively. Thus, the thickness of the thin film increases with increasing Fe₂O₃ sputtering time.

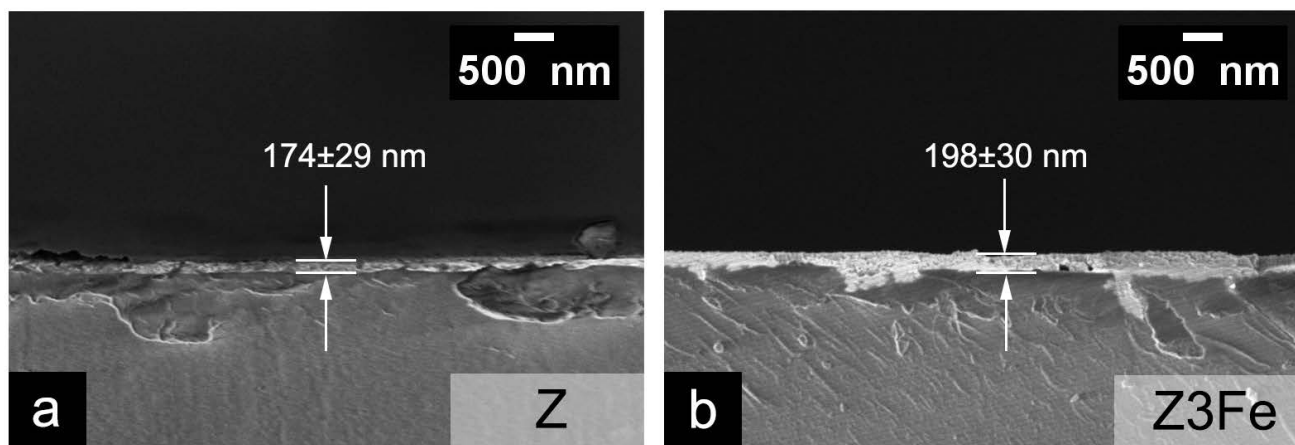


Figure 6. SEM microphotographs of chips of Z (a) and Z3Fe (b) samples on glass substrates.

Considering all of the above data (EDX, SEM, XRD, Raman, XPS) on the phase composition, microstructure, dispersity, and thickness of the obtained ZnO/Fe₂O₃ films, the following conclusions can be made. At the minimum deposition time of Fe₂O₃ (10 min, sample Z1Fe), Fe₂O₃ coating is formed on the surface of ZnO, consisting of individual clusters of nanoparticles, which seemingly do not constitute a continuous coating. When the Fe₂O₃ deposition time is increased up to 20–30 min (samples Z2Fe and Z3Fe), a thin continuous Fe₂O₃ coating with a thickness of about 10–20 nm with an average nanoparticle size of 23–28 nm begins to form on the ZnO surface. Thus, by varying the time of deposition of the modifying layer, it is possible to change the continuity and thickness of the obtained

coating. Table 1 summarizes the properties of the obtained ZnO/Fe₂O₃ nanostructured thin films.

Table 1. Various characteristics of the obtained ZnO/Fe₂O₃ nanostructured thin films.

Sample	Content Fe, at. %	Average Crystallite Size (L), nm	Average Particle Size of ZnO, nm	Average Particle Size of Fe ₂ O ₃ , nm	Average Film Thickness, nm	Eg, eV	Response (S) to 300–2000 ppb NO ₂	Selectivity Coefficient (Sel)	Response Drop (RD) at 25–75%RH	Response Time, c
Z	0	40	66	-	174	3.26	1.3–4.0	1.2	11.1–15.6	143–180
Z1Fe	1.3	42	50	-	181	3.26	4.0–14.2	3.4	4.2–12.8	118–203
Z2Fe	4.8	30	51	23	185	3.23	1.9–6.1	1.7	9.3–21.9	121–160
Z3Fe	5.8	35	-	28	198	3.16	1.3–2.6	0.6	16.7–36.7	58–176

3.3. UV Transmittance Spectra and Optical Band Gap

Figure 7a shows spectra of UV and visible transmittance of the films on glass substrates. It can be seen from the data that all films have a high transmittance in the visible range. The transmittance of Z and Z1Fe films ranges from 87 to 97% of visible light, Z1Fe—90–97%, and Z3Fe has the lowest transmittance in the visible range (90–92%), probably due to the dense coating of ZnO surface with Fe₂O₃ nanoparticles. The edge of the fundamental absorption band of the films corresponds to the transition of the electron from the valence band to the conduction band, and it can be used to calculate the optical band gap width. The optical band gap width was determined by plotting the Tauc plot (Figure 7b) [55]. The Eg values of ZnO/Fe₂O₃ films calculated by this method are 3.26, 3.26, 3.23, and 3.16 eV for samples Z, Z1Fe, Z2Fe, and Z3Fe, respectively. The narrowing of the band gap width can be explained by the strength of ionic bonding between metal ions and oxygen ions. The electronegativity values of Zn, Fe, and O are 1.5, 1.8, and 3.5, respectively [56], so the difference in energy levels between the s-state cation and the O 2p state in α -Fe₂O₃ is smaller than in ZnO. This testifies to the fact that the red shift of the absorption edge occurs mainly due to the formation of Fe s-levels below the conduction zone of ZnO [57].

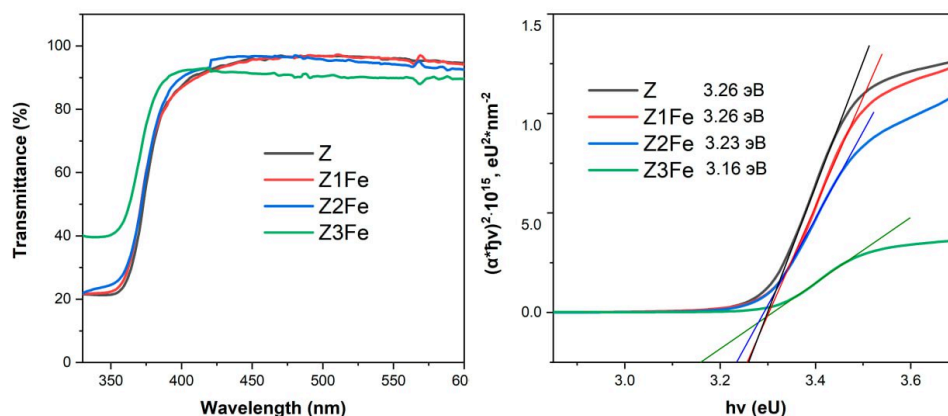


Figure 7. UV transmittance spectra (a) and Tauc plot (b) for thin films of ZnO/Fe₂O₃.

3.4. Gas-Sensing Chemoresistive Properties

3.4.1. Selectivity

The obtained ZnO/Fe₂O₃ films showed good electrical conductivity, which allowed us to study chemoresistance responses to various gases (H₂, CH₄, CO, C₆H₆, NH₃, ethanol, acetone, and NO₂) in a wide temperature range: from 150 to 300 °C (Figure 8).

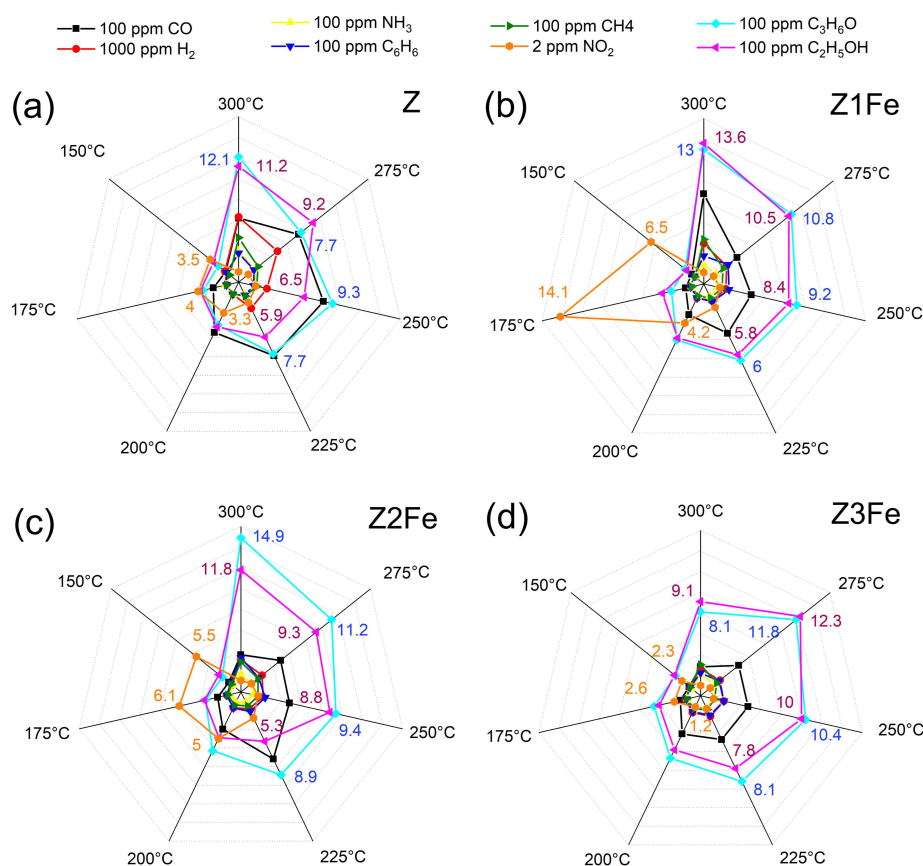


Figure 8. Selectivity diagrams responses to various gases (H₂, CH₄, CO, C₆H₆, NH₃, ethanol, acetone, and NO₂) at 150–300 °C of the samples: (a) Z, (b) Z1Fe, (c) Z2Fe, and (d) Z3Fe.

At lower operating temperatures, the resistance of the nanocomposite films was high enough that it was not possible to evaluate the gas sensitivity on the equipment used in the present work (electrical resistance measurements were limited to 1 GOhm). At elevated temperatures, the greatest response for all analyzed films was observed for VOCs: ethanol and acetone. The greatest sensitivity to the above gases was observed at 300 °C, with response values being: 11.2, 13.6, and 11.8 (100 ppm ethanol), as well as 12.1, 13.0, and 14.9 (100 ppm acetone) for samples Z, Z1Fe, and Z2Fe, respectively. For the sample with the highest iron content (Z3Fe), the maximum response (11.8 and 12.3 for ethanol and acetone, respectively) was observed at 275 °C. The response to other gases at 275–300 °C did not exceed 7.4, 8.7, 4.9, and 4.7 for Z, Z1Fe, Z2Fe, and Z3Fe, respectively. Upon lowering the operating temperature to 150 °C, a significant decrease in the responses to ethanol and acetone (to 2.1–3.2) was observed. When detecting NO₂, a different dependence was observed: when the operating temperature was changed from 300 to 150 °C, the response significantly increased. Such phenomena are quite typical for ZnO-based receptor nanomaterials, which are characterized by increased sensitivity to various VOCs at elevated temperatures and to NO₂ at moderate ones [58,59].

To select the optimal temperature for the detection of the analyte gas, several factors should be taken into account, among which the main ones are, definitely, selectivity and energy efficiency, which are determined by the operating temperatures at which the detection is performed. When analyzing the obtained array of responses of ZnO/Fe₂O₃ thin films to various gases at 150–300 °C, a low working temperature of 175 °C was chosen, and pronounced sensitivity to ultra-low NO₂ concentrations was observed at this point. Next, the chemoresistive gas-sensitive properties upon NO₂ detection at 175 °C were studied in more detail (Figure 9).

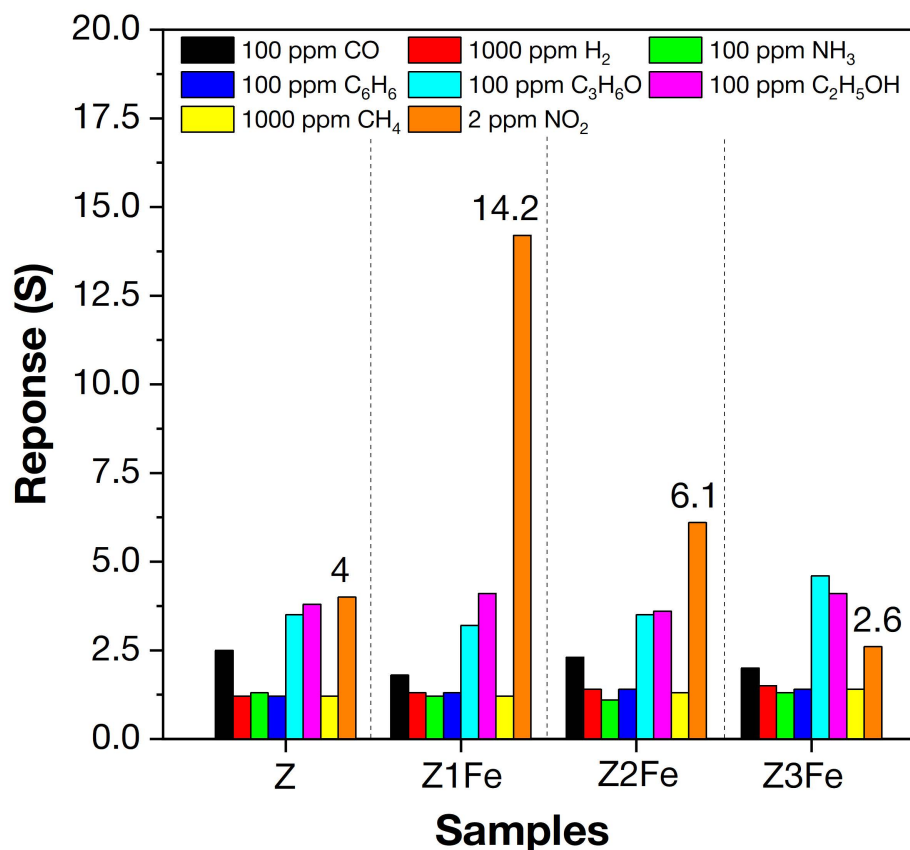


Figure 9. Selectivity histogram of the samples to various gases (H₂, CH₄, CO, C₆H₆, NH₃, ethanol, acetone, and NO₂) at 175 °C.

All samples of ZnO/Fe₂O₃ thin films showed unusually high sensitivity to NO₂. An increase in electrical resistance (which is typical for n-type MOS) was observed when detecting NO₂. When the concentration of NO₂ increases above 2 ppm, the resistance upon response recording exceeds 1 GOhm, which does not allow its detection on the equipment used. Therefore, all further measurements upon NO₂ detection were limited to the concentration of 2 ppm. The sample (Z1Fe) with the lowest iron content had the highest response ($S = 14.2$) and selectivity ($Sel = 3.4$) when detecting 2 ppm NO₂. For other samples, the responses to 2 ppm NO₂ are 4.0, 6.1, and 2.6, and the selectivity coefficients were 1.2, 1.7, and 0.6 for Z, Z2Fe, and Z3Fe, respectively. Thus, the sample (Z1Fe) with the lowest iron content has the highest selectivity at 2 ppm NO₂. It should be noted that the comparison of responses to NO₂ with other gases was carried out at their various concentrations, which differ by 50 times or more (100 ppm vs. 2 ppm NO₂). Therefore, the obtained value ($Sel = 3.4$) for Z1Fe, as well as for other samples, is an extremely high value, showing good selectivity for NO₂ detection.

Figure 10a shows the experimental data on the sensitivity to different NO₂ concentrations of Z, Z1Fe, Z2Fe, and Z3Fe samples. The zinc oxide-based films show a high response in a wide range of ultra-low NO₂ concentrations (300–2000 ppb), covering the threshold limit value (TLV) recommended by the National Institute for Occupational Safety and Health [60]. The response increases from 1.3 to 4.0, 4.0–14.2, 1.9–6.1, and 1.3–2.6 with increasing NO₂ concentrations from 300 to 2000 ppb for Z, Z1Fe, Z2Fe, and Z3Fe, respectively.

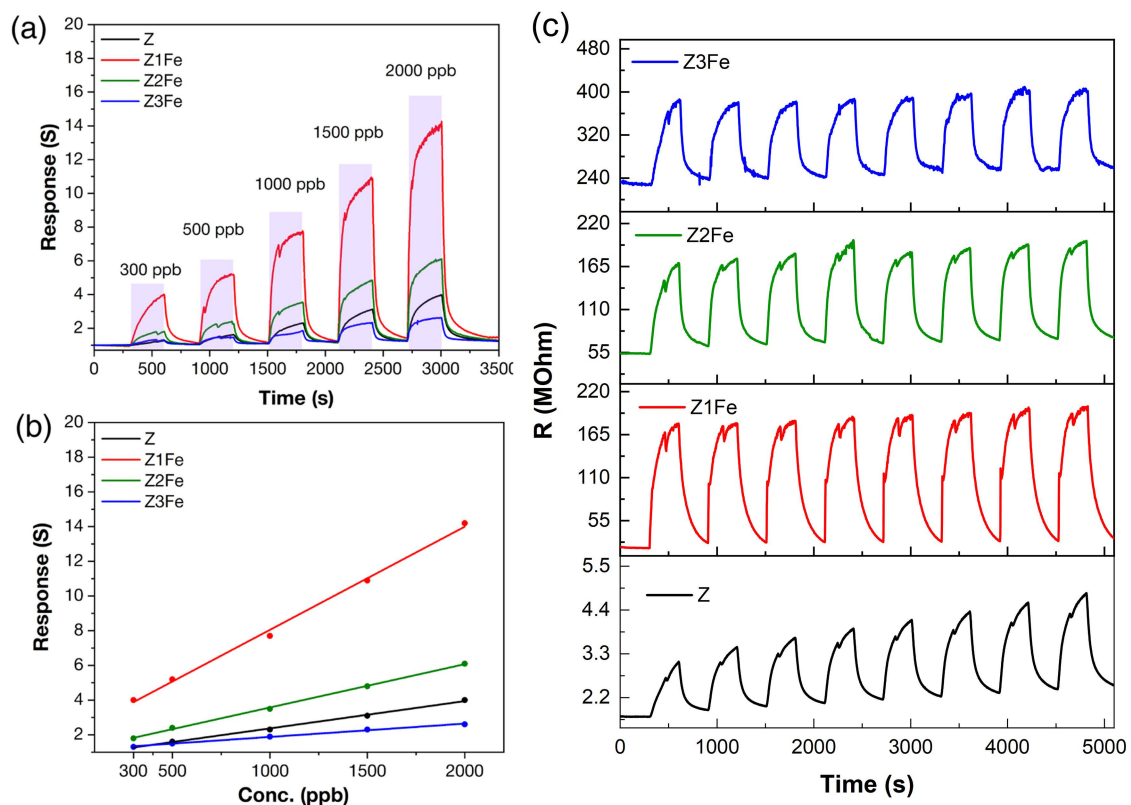


Figure 10. Sensitivity to 300–2000 ppb NO₂ (a); dependences of response from NO₂ concentration (b) and reproducibility of the signal when detecting 500 ppb NO₂ (c) at 175 °C operating temperature and 0%RH for ZnO/Fe₂O₃ thin films.

Figure 10b shows the dependences of the response value on the concentration of NO₂ in the gas mixture. The highest response over the entire NO₂ concentration range was observed for the Z1Fe sample. All samples can be described well by a linear function. This dependence is typical for many chemoresistive gas sensors and correlates well with the available literature data [1,61]. Figure 10c shows the reproducibility of the signal when detecting 500 ppb NO₂ at 0%RH. It can be seen that, for individual ZnO, there is a drift in the values. With the addition of iron, the signal becomes more stable with minimal drift of the resistance values.

The kinetic characteristics were evaluated: the response time changes nonlinearly with increasing analyte concentration, and, for concentrations of 300–2000 ppb, these values amount to 143–180, 118–203, and 121–160, as well as 58–176 s for Z, Z1Fe, Z2Fe, and Z3Fe, respectively.

Figure 11 shows the responses of samples Z, Z1Fe, Z2Fe, and Z3Fe when detecting 500 ppb NO₂ at different relative humidity values (RH). For individual ZnO, when the RH increases from 0 to 75%, a consistent decrease in the response value from 1.8 to 1.5 is observed (Figure 11a). The shape of the signal has a sharply pointed appearance, which may indicate that the equilibrium on the surface has not been established, which is due to the long process of establishing a stable signal. When doped with iron oxide, the shape of the responses becomes close to rectangular. For the sample Z1Fe (Figure 11b), the smallest influence of humidity on the signal is observed. At RH in the 0–75% range, the response decreases linearly from 4.6 to 4.1. The Z2Fe sample (Figure 11c) shows a response of 3.2–2.4 with a general trend of decreasing response with increasing humidity, but the signal at 50% RH is slightly greater than at 25% RH. A different behavior is exhibited by Z3Fe (Figure 8d), for which the response in a humid environment (2.3–2.5) is higher than in a dry atmosphere (1.8).

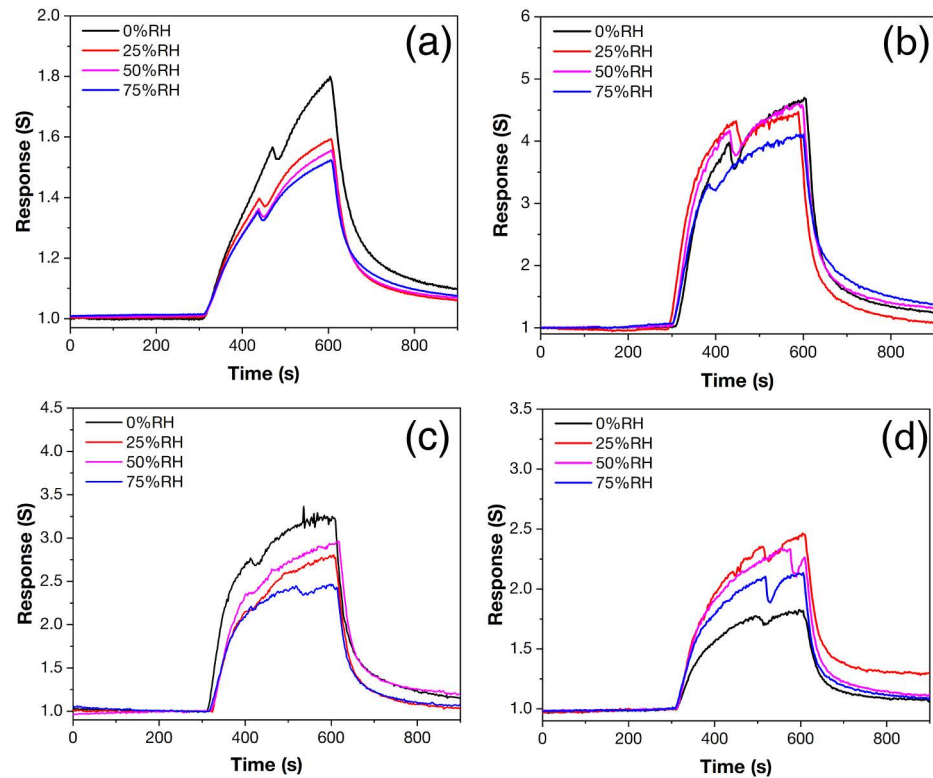


Figure 11. Response to 500 ppb NO₂ at 175 °C and 0–75% RH of ZnO/Fe₂O₃ thin films: Z (a), Z1Fe (b), Z2Fe (c), and Z3Fe (d).

Figure 12a summarizes the data on the effect of humidity on the response value of the obtained thin films. For samples Z, Z1Fe, and Z2Fe, the response dependence on RH can be described by the curve with a negative slope. The sample Z3Fe showed an increase in the response at 25% RH, and then a consistent decrease in its value was observed. Figure 12b shows the modulus of change in the response value relative to its value in dry air. As can be seen, the sample Z1Fe is the least affected by humidity among the samples, and the sample Z3Fe has the maximum sensitivity to humidity.

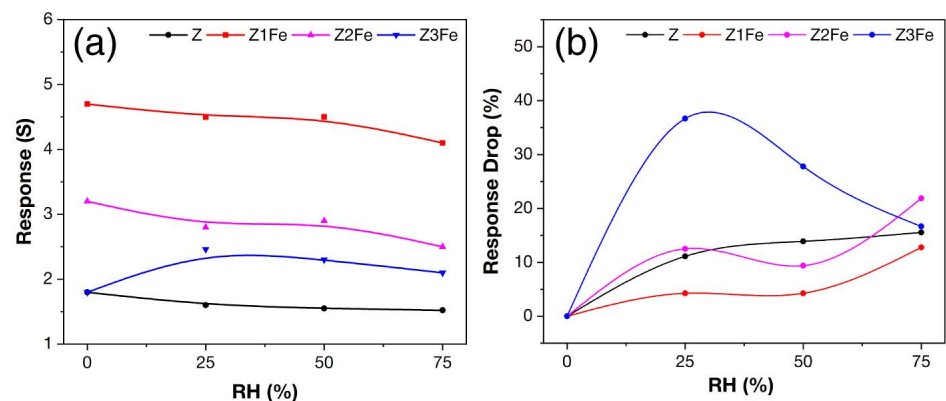


Figure 12. Dependence of response value on humidity (a) and response drop (RD) in a humid environment (b) when detecting 500 ppb NO₂ at 175 °C with ZnO/Fe₂O₃ thin films.

3.4.2. Detection Mechanism

The resistive response in the detection of NO₂ by individual ZnO results from various reactions, which can be described using the model for n-type semiconductors generally accepted in the literature. In an air environment at elevated temperatures, oxygen molecules adsorb onto the semiconductor surface, which leads to a change in the resistance of the

material. Electrons from the conduction zone reduce O_2 to ionic form (at 175 °C, O^- particles would be predominant) [62]. The presence of such ions on the ZnO surface contributes to the formation of the electronic structure of the core–shell type. The core is the inner region of the semiconductor particle, and the shell is the electron depletion layer (EDL) formed as a result of electron consumption during the reduction of O_2 to O^- .

In the work by Mei Chen et al. [63], the process of interaction of NO_2 with zinc oxide was studied using a number of methods of in situ physicochemical analysis. The authors were able to show that, upon the intake of NO_2 , nitrites (NO_2^-) and then nitrates (NO_3^-) are formed in the first minutes with the participation of various defects in the crystal lattice of ZnO. The formation of NO_2^- (ads) and NO_3^- (ads) can also occur with the participation of electrons from the conduction band of ZnO, the lattice oxygen $O_{(lat)}$ or the sorbed O^- (ads) ion [64]. In our previous work [59], while studying the thick zinc oxide films obtained by solvothermal method, we correlated the Mei Chen data with the results we obtained in the study of chemoresistive responses in NO_2 detection and summarized them. More details on the mechanisms of NO_2 detection by individual ZnO can be found in our work at the above reference.

Thus, based on the above data, we can conclude that the maximum response to NO_2 of an individual ZnO thin film at 175 °C can be explained by the maximum intensity of NO_2 adsorption in this temperature range. It is worth noting that, just as in our previous work, where a thick ZnO film was obtained by the solvothermal method, so in the present work, where a thin ZnO film was obtained by the AACVD method, zinc acetylacetonate was used as a precursor. In both cases, extremely NO_2 -sensitive receptor nanomaterials, based on ZnO, were obtained using completely different methods. Therefore, the choice of the precursor used probably also plays an important role in obtaining a highly sensitive receptor nanomaterial for chemoresistive gas sensors.

The highest response over the entire NO_2 concentration range for the Z1Fe sample can be attributed to the formation of a heterojunction (Figure 13). The Fermi level of Fe_2O_3 is lower than that of ZnO, so there is directional electron transfer from the conduction zone of ZnO to Fe_2O_3 until level alignment is achieved. Thus, an electron-depleted layer is formed at the boundary of the two semiconductors, which leads to significant chemical and electronic sensitization. In addition, the Fe_2O_3 nanoparticles can interact with NO_2 , which leads to the electron transfer from ZnO to Fe_2O_3 and widening of the electron-depleted ZnO layer [65]. The obtained cluster structure of Fe_2O_3 nanoparticles on the ZnO surface (sample Z1Fe) is suitable for the realization of the heterojunction, as described above, allowing us to improve the chemoresistive properties. As the thickness of the Fe_2O_3 layer increases, the sensitivity to NO_2 decreases as the area covered by the Fe_2O_3 nanoparticles increases. Zinc oxide stops being the main gas-sensitive material, and the heterojunction effect ceases to be the limiting one.

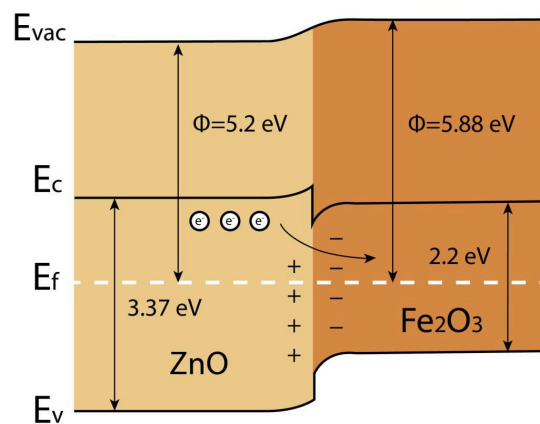
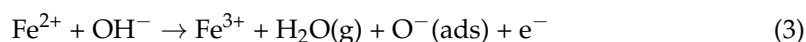


Figure 13. Energy diagram of heterojunction formation between ZnO and Fe_2O_3 in ZnO/ Fe_2O_3 thin films.

In humid atmosphere, water molecules sorbed on the ZnO surface additionally participate in the detection mechanism. In many cases, humidity has a negative effect on the chemoresistive response and remains one of the main problems in gas sensing. After sorption, the H₂O(ads) molecules react with point defects (zinc Zn(lat) and oxygen O(lat) in the crystal lattice, resulting in the formation of hydroxyl groups on the ZnO surface [3,66]. The released electrons enter the conduction band of ZnO, which leads to decrease in electrical resistance. The formed hydroxyl groups occupy the active adsorption centers on the ZnO surface, thus reducing the adsorption of NO₂(ads) and O⁻(ads) and the intensity of the reactions, which contribute to a chemoresistive response.

For the sample Z1Fe with the Fe₂O₃ cluster structure, moisture has almost no effect on the response value. Additionally, with further increase in the thickness of the Fe₂O₃ layer, on the contrary, the largest drop in the response is observed. It can be assumed that, when doping with Fe₂O₃, the observed phenomena are related to the participation of iron cations directly on the surface of the ZnO film in the detection mechanism. Iron in oxides is known in two stable oxidation degrees: +2 and +3, which correspond to the oxides FeO, Fe₂O₃, and Fe₃O₄. After sorption of water molecules, we can assume the following reactions of iron cations with hydroxyl groups:



Thus, a small iron content contributes to leveling the influence of moisture. With further increase in the iron content, reactions (3–4) begin to compete with those resulting in a response to NO₂, which leads to an increase in the response drop. Nevertheless, this mechanism has not been experimentally confirmed and requires further study.

3.4.3. ZnO/Fe₂O₃ Nanostructured Thin Films As Gas Biosensors

The obtained ZnO/Fe₂O₃ thin-film nanocomposites showed extremely high sensitivity to ultra-low NO₂ concentrations (300–2000 ppb). Nitrogen dioxide is a gas biomarker for diseases associated with inflammatory processes in the lungs: bronchial asthma, bronchiectasis, and chronic obstructive pulmonary disease (COPD) [32,36,37]. The concentration of NO_x in the exhaled air of a sick person, compared to the exhaled air of a healthy person, differs at the level of tens of ppb. Thus, the detection limit of NO₂ by the ZnO/Fe₂O₃ thin-film nanocomposites obtained in the present work is not only much lower than the TLV, which is important in the context of environmental safety, but is also in a suitable range for medical purposes. Therefore, ZnO/Fe₂O₃ nanocomposites can be effective receptor materials in the composition of analytical devices for noninvasive diagnosis of diseases related to lung disease.

Additionally, to enable selective signal separation, we used principal component analysis (PCA) to evaluate the correlation between the response of the four receptor nanomaterials used (Z, Z1Fe, Z2Fe and Z3Fe) and selectivity. Chemometric analysis is quite common in multisensor and E-nose systems for the detection of a wide group of analyte gases, including medical applications. Figure 14 shows the data obtained after mathematical processing of the PCA responses using the covariance matrix. As can be seen, the resulting graph consists of several distant clusters: 300–2000 ppb NO₂, 100 ppm C₂H₅OH, C₃H₆O, and CO, and 1000 ppm CH₄, H₂, 100 ppm C₆H₆, and NH₃ (inset), which allows their concentrations to be determined with high accuracy. Thus, using a sensor array consisting of four thin-film ZnO/Fe₂O₃ nanocomposites, signals can be separated with great selectivity when detecting the eight diverse analyte gases used in this work. Such results are extremely important in the transition to multisensor devices that are used for noninvasive disease diagnosis, where it is necessary to analyze a wide group of gases contained in human exhaled air.

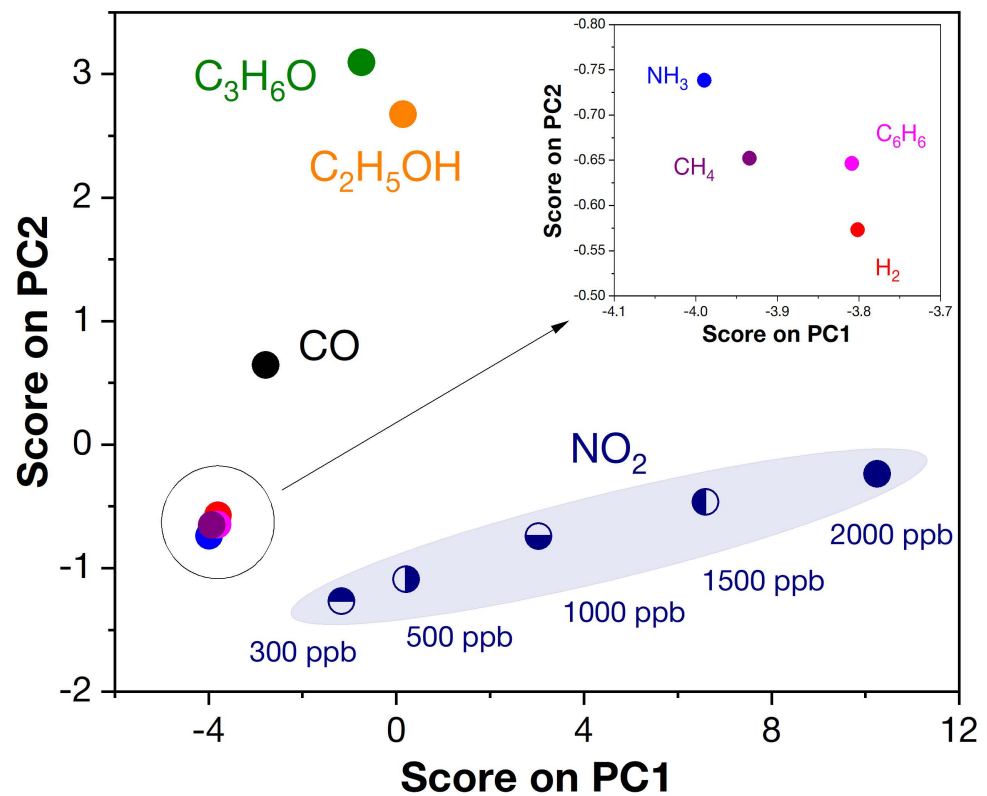


Figure 14. Pattern recognition based on PCA analysis for ZnO/Fe₂O₃ thin film nanocomposites.

Table 2 compares some gas-sensitive characteristics of ZnO/Fe₂O₃ nanocomposites with analogues presented in the literature. It is worth noting that the ZnO/Fe₂O₃ thin films obtained in our work have an improved set of gas-sensing properties: moderately low detection temperature, low detection limit, high response, and good selectivity.

Table 2. Comparison of gas sensing properties of various ZnO-Fe₂O₃-based composites sensors in present work and literatures.

Composition	Synthesis/Coating Method	Gas	Conc, ppm	Temp, °C	Response	Response Time (s)	Selectivity	Ref.
α-Fe ₂ O ₃ -ZnO	Hydrothermal method	NO ₂	10	300	6.34	26	-	[67]
ZnO-Fe ₂ O ₃	Co-precipitation method	NO ₂	250	400	10.53	1000	-	[68]
ZnFe ₂ O ₄ nanosheets	Soaking, freeze-drying and calcination	Acetone	50	220	64.9	23	1.6	[69]
α-Fe ₂ O ₃ -ZnO core-shell nanowires	thermal oxidation/ ALD	H ₂ S	5	250	5.98	81	5.2	[70]
Fe ₂ O ₃ -ZnO Nanograins	solid-state reaction method/RF magnetron sputtering	H ₂ O ₂	1.5	RT + UV	12	91	4.9	[71]
Fe ₂ O ₃ -ZnO	solid-state reaction method/RF magnetron sputtering	NH ₃	548	250	6	~70	-	[72]
Fe ₂ O ₃ -ZnO	solid-state reaction method/RF magnetron sputtering	H ₂	2000	100	5045	372	>40	[73]
ZnO/α-Fe ₂ O ₃ core-shell nanorods	chemical solution method/ionic-layer adsorption and reaction method	Ethanol	400	240	39	8	~4.9	[1]
ZnO-Fe ₂ O ₃	solvothermal method	Acetone	100	290	29.9	-	1.4	[24]
ZnO-Fe ₂ O ₃	thermal evaporation/solvothermal deposition	Ethanol	2000	200	~70	~115	-	[23]
tetrapod ZnO doped with Fe ₂ O ₃	flame transport synthesis/ annealing with Fe	Ethanol	100	RT	51	2.5	20.4	[25]
ZnO-Fe ₂ O ₃	vapor-liquid-solid process/sol-gel process	CO	100	300	18.8	~200	3	[26]
ZnO-Fe ₂ O ₃	AACVD	NO ₂	2	175	14.2	118	3.4	This work

4. Conclusions

ZnO/ α -Fe₂O₃ nanocomposites were prepared by two-step aerosol vapor deposition (AACVD). Zinc and iron acetylacetonates in methanol were used as precursors, and synthesis was carried out at 400 °C with sequential sputtering of ZnO (60 min) and Fe₂O₃ (10, 20, 30 min). The iron content of the films with sputtering times of 10, 20, and 30 min was found to be 1.3, 4.8, and 5.8 at%, respectively, according to EDX data. The phase composition was determined by Raman spectroscopy, XPS and XRD were used for analysis, and the morphology was determined by SEM. ZnO particles have a wurtzite structure with an average size of 51–66 nm, and iron oxide particles with hematite structure on the surface of ZnO have an average size of 23–28 nm. All films have a large transmittance in the visible range. The optical band gap calculated by the Tauc method decreases with increasing Fe₂O₃ concentration from 3.26 to 3.16 eV. The films obtained showed a high response to 100 ppm acetone and ethanol at 225–300 °C and a high and selective response to 300–2000 ppb NO₂ at 175 °C. The effect of humidity on the magnitude and shape of the signal obtained in NO₂ detection was studied. The sensor with 1.3 at% Fe has the highest response, selectivity coefficient, and it has lower dependence on humidity, which can be explained by the formation of a heterojunction at the boundary of the two semiconductors.

Author Contributions: Conceptualization, A.S.M., Y.M.G. and E.P.S.; methodology, N.T.K.; validation, E.P.S. and N.T.K.; investigation, A.S.M., P.Y.G., A.A.A., N.P.S. and Y.Y.L.; resources, N.T.K.; writing—original draft preparation, A.S.M., Y.M.G. and P.Y.G.; writing—review and editing Y.M.G., A.A.A., N.P.S., Y.Y.L. and E.P.S.; supervision, N.T.K.; project administration, A.S.M.; funding acquisition, A.S.M. All authors have read and agreed to the published version of the manuscript.

Funding: The study of the gas-sensing properties was supported by a grant of the President of the Russian Federation (grant no. MK-2276.2022.1.3). The development of the methods for the synthesis of semiconductor receptor oxide nanomaterials was supported by the Ministry of Science and Higher Education of the Russian Federation under a state assignment for the Kurnakov Institute of General and Inorganic Chemistry, Russian Academy of Sciences, Moscow, Russia (IGIC RAS). The microstructure and phase composition of the samples were studied using equipment of the Center for Shared Use of Physical Methods of Investigation of Substances and Materials, IGIC RAS, the work of which is supported by the Ministry of Science and Higher Education of the Russian Federation under a state assignment for IGIC RAS.

Institutional Review Board Statement: Not applicable.

Informed Consent Statement: Not applicable.

Data Availability Statement: Not applicable.

Conflicts of Interest: The authors declare no conflict of interest.

References

1. Zhang, B.; Fu, W.; Meng, X.; Ruan, A.; Su, P.; Yang, H. Synthesis and Enhanced Gas Sensing Properties of Flower-like ZnO/ α -Fe₂O₃ Core-Shell Nanorods. *Ceram. Int.* **2017**, *43*, 5934–5940. [[CrossRef](#)]
2. Deng, Y. *Semiconducting Metal Oxides for Gas Sensing*; Elsevier: Amsterdam, The Netherlands, 2019; ISBN 9789811358524.
3. Hsu, C.L.; Chang, L.F.; Hsueh, T.J. Light-Activated Humidity and Gas Sensing by ZnO Nanowires Grown on LED at Room Temperature. *Sens. Actuators B Chem.* **2017**, *249*, 265–277. [[CrossRef](#)]
4. Kang, Y.; Yu, F.; Zhang, L.; Wang, W.; Chen, L.; Li, Y. Review of ZnO-Based Nanomaterials in Gas Sensors. *Solid State Ion.* **2021**, *360*, 115544. [[CrossRef](#)]
5. Ma, T. Effect of Precursor Concentration and Sintering on Functional Properties of ZnO Thin Films Deposited by Aerosol-Assisted Chemical Vapour Deposition (AACVD). *Mater. Sci. Semicond. Process.* **2021**, *121*, 105413. [[CrossRef](#)]
6. Zhang, B.; Fu, W.; Li, H.; Fu, X.; Wang, Y.; Bala, H.; Sun, G.; Wang, X.; Wang, Y.; Cao, J.; et al. Actinomorphic ZnO/SnO₂ Core-Shell Nanorods: Two-Step Synthesis and Enhanced Ethanol Sensing Properties. *Mater. Lett.* **2015**, *160*, 227–230. [[CrossRef](#)]
7. Bai, S.; Guo, T.; Zhao, Y.; Sun, J.; Li, D.; Chen, A.; Liu, C.C. Sensing Performance and Mechanism of Fe-Doped ZnO Microflowers. *Sens. Actuators B Chem.* **2014**, *195*, 657–666. [[CrossRef](#)]
8. Ganbavle, V.V.; Inamdar, S.I.; Agawane, G.L.; Kim, J.H.; Rajpure, K.Y. Synthesis of Fast Response, Highly Sensitive and Selective Ni:ZNO Based NO₂ Sensor. *Chem. Eng. J.* **2016**, *286*, 36–47. [[CrossRef](#)]

9. Wang, C.N.; Li, Y.L.; Gong, F.L.; Zhang, Y.H.; Fang, S.M.; Zhang, H.L. Advances in Doped ZnO Nanostructures for Gas Sensor. *Chem. Rec.* **2020**, *20*, 1553–1567. [[CrossRef](#)]
10. Sankar Ganesh, R.; Durgadevi, E.; Navaneethan, M.; Patil, V.L.; Ponnusamy, S.; Muthamizhchelvan, C.; Kawasaki, S.; Patil, P.S.; Hayakawa, Y. Low Temperature Ammonia Gas Sensor Based on Mn-Doped ZnO Nanoparticle Decorated Microspheres. *J. Alloys Compd.* **2017**, *721*, 182–190. [[CrossRef](#)]
11. Chang, C.J.; Lin, C.Y.; Chen, J.K.; Hsu, M.H. Ce-Doped ZnO Nanorods Based Low Operation Temperature NO₂ Gas Sensors. *Ceram. Int.* **2014**, *40*, 10867–10875. [[CrossRef](#)]
12. Zhang, X.H.; Chen, J.; Wu, Y.; Xie, Z.; Kang, J.; Zheng, L. A Simple Route to Fabricate High Sensibility Gas Sensors Based on Erbium Doped ZnO Nanocrystals. *Colloids Surfaces A Physicochem. Eng. Asp.* **2011**, *384*, 580–584. [[CrossRef](#)]
13. Kim, J.H.J.Y.; Lee, J.H.; Park, Y.; Kim, J.H.J.Y.; Mirzaei, A.; Kim, H.W.; Kim, S.S. Toluene- and Benzene-Selective Gas Sensors Based on Pt- and Pd-Functionalized ZnO Nanowires in Self-Heating Mode. *Sens. Actuators B Chem.* **2019**, *294*, 78–88. [[CrossRef](#)]
14. Postica, V.; Vahl, A.; Santos-Carballeda, D.; Dankwort, T.; Kienle, L.; Hoppe, M.; Cadi-Essadek, A.; De Leeuw, N.H.; Terasa, M.I.; Adelung, R.; et al. Tuning ZnO Sensors Reactivity toward Volatile Organic Compounds via Ag Doping and Nanoparticle Functionalization. *ACS Appl. Mater. Interfaces* **2019**, *11*, 31452–31466. [[CrossRef](#)]
15. Hosseini, Z.S.; Mortezaali, A.; Iraj Zad, A.; Fardindoost, S. Sensitive and Selective Room Temperature H₂S Gas Sensor Based on Au Sensitized Vertical ZnO Nanorods with Flower-like Structures. *J. Alloys Compd.* **2015**, *628*, 222–229. [[CrossRef](#)]
16. Yadav, A.A.; Lokhande, A.C.; Kim, J.H.; Lokhande, C.D. Improvement in CO₂ Sensing Characteristics Using Pd Nanoparticles Decorated La₂O₃ Thin Films. *J. Ind. Eng. Chem.* **2017**, *49*, 76–81. [[CrossRef](#)]
17. Hsu, K.C.; Fang, T.H.; Hsiao, Y.J.; Li, Z.J. Rapid Detection of Low Concentrations of H₂S Using CuO-Doped ZnO Nanofibers. *J. Alloys Compd.* **2021**, *852*, 157014. [[CrossRef](#)]
18. Qu, Z.; Fu, Y.; Yu, B.; Deng, P.; Xing, L.; Xue, X. High and Fast H₂S Response of NiO/ZnO Nanowire Nanogenerator as a Self-Powered Gas Sensor. *Sens. Actuators B Chem.* **2016**, *222*, 78–86. [[CrossRef](#)]
19. Franco, M.A.; Conti, P.P.; Andre, R.S.; Correa, D.S. A Review on Chemiresistive ZnO Gas Sensors. *Sens. Actuators Rep.* **2022**, *4*, 100100. [[CrossRef](#)]
20. Andre, R.S.; Pereira, J.C.; Mercante, L.A.; Locilento, D.; Mattoso, L.H.C.; Correa, D.S. ZnO-Co₃O₄ Heterostructure Electrospun Nanofibers Modified with Poly(Sodium 4-Styrenesulfonate): Evaluation of Humidity Sensing Properties. *J. Alloys Compd.* **2018**, *767*, 1022–1029. [[CrossRef](#)]
21. Zhang, J.; Liu, X.; Wang, L.; Yang, T.; Guo, X.; Wu, S.; Wang, S.; Zhang, S. Synthesis and Gas Sensing Properties of α -Fe₂O₃@ZnO Core-Shell Nanospindles. *Nanotechnology* **2011**, *22*, 185501. [[CrossRef](#)]
22. Mirzaei, A.; Hashemi, B.; Janghorban, K. α -Fe₂O₃ Based Nanomaterials as Gas Sensors. *J. Mater. Sci. Mater. Electron.* **2016**, *27*, 3109–3144. [[CrossRef](#)]
23. Kim, S.; Park, S.; Kheel, H.; Lee, W.I.; Lee, C. Enhanced Ethanol Gas Sensing Performance of the Networked Fe₂O₃-Functionalized ZnO Nanowire Sensor. *J. Nanosci. Nanotechnol.* **2016**, *16*, 8585–8588. [[CrossRef](#)]
24. Zhou, X.; Xiao, Y.; Wang, M.; Sun, P.; Liu, F.; Liang, X.; Li, X.; Lu, G. Highly Enhanced Sensing Properties for ZnO Nanoparticle-Decorated Round-Edged α -Fe₂O₃ Hexahedrons. *ACS Appl. Mater. Interfaces* **2015**, *7*, 8743–8749. [[CrossRef](#)]
25. Lupan, O.; Postica, V.; Gröttrup, J.; Mishra, A.K.; de Leeuw, N.H.; Adelung, R. Enhanced UV and Ethanol Vapour Sensing of a Single 3-D ZnO Tetrapod Alloyed with Fe₂O₃ Nanoparticles. *Sens. Actuators B Chem.* **2017**, *245*, 448–461. [[CrossRef](#)]
26. Jeongseok, L.; Se-Hyeong, L.; So-Young, B.; Yoojong, K.; Kyoungwan, W.; Sanghyun, L.; Yooseong, L.; Moonsuk, Y. Improved Sensitivity of α -Fe₂O₃ Nanoparticle-Decorated ZnO Nanowire Gas Sensor for CO. *Sensors* **2019**, *19*, 1903. [[CrossRef](#)]
27. Iram, S.; Mahmood, A.; Ehsan, M.F.; Mumtaz, A.; Sohail, M.; Sitara, E.; Mushtaq, S.; Malik, M.A.; Fatima, S.A.; Shaheen, R.; et al. Impedance Spectroscopy Analysis of Pbse Nanostructures Deposited by Aerosol Assisted Chemical Vapor Deposition Approach. *Nanomaterials* **2021**, *11*, 2817. [[CrossRef](#)]
28. Knapp, C.E.; Carmalt, C.J. Solution Based CVD of Main Group Materials. *Chem. Soc. Rev.* **2016**, *45*, 1036–1064. [[CrossRef](#)]
29. Shukla, A.; Kaushik, V.K.; Prasher, D. Growth and Characterization of Mg_xZn_{1-x}O Thin Films by Aerosol-Assisted Chemical Vapor Deposition (AACVD). *Electron. Mater. Lett.* **2014**, *10*, 61–65. [[CrossRef](#)]
30. Potter, D.B.; Parkin, I.P.; Carmalt, C.J. The Effect of Solvent on Al-Doped ZnO Thin Films Deposited via Aerosol Assisted CVD. *RSC Adv.* **2018**, *8*, 33164–33173. [[CrossRef](#)]
31. Claros, M.; Setka, M.; Jimenez, Y.P.; Vallejos, S. Aacvd Synthesis and Characterization of Iron and Copper Oxides Modified ZnO Structured Films. *Nanomaterials* **2020**, *10*, 471. [[CrossRef](#)]
32. Corradi, M.; Majori, M.; Cacciani, G.C.; Consigli, G.F.; De'Munari, E.; Pesci, A. Increased Exhaled Nitric Oxide in Patients with Stable Chronic Obstructive Pulmonary Disease. *Thorax* **1999**, *54*, 572–575. [[CrossRef](#)]
33. Wilson, A.D. Advances in Electronic-Nose Technologies for the Detection of Volatile Biomarker Metabolites in the Human Breath. *Metabolites* **2015**, *5*, 140–163. [[CrossRef](#)] [[PubMed](#)]
34. van der Sar, I.G.; Wijbenga, N.; Nakshbandi, G.; Aerts, J.G.J.V.; Manintveld, O.C.; Wijzenbeek, M.S.; Hellemons, M.E.; Moor, C.C. The Smell of Lung Disease: A Review of the Current Status of Electronic Nose Technology. *Respir. Res.* **2021**, *22*, 1–22. [[CrossRef](#)] [[PubMed](#)]
35. Yang, D.; Gopal, R.A.; Lkhagvaa, T.; Choi, D. Metal-Oxide Gas Sensors for Exhaled-Breath Analysis: A Review. *Meas. Sci. Technol.* **2021**, *32*, 102004. [[CrossRef](#)]

36. Smith, A.D.; Cowan, J.O.; Filsell, S.; McLachlan, C.; Monti-Sheehan, G.; Jackson, P.; Taylor, D.R. Diagnosing Asthma: Comparisons between Exhaled Nitric Oxide Measurements and Conventional Tests. *Am. J. Respir. Crit. Care Med.* **2004**, *169*, 473–478. [[CrossRef](#)] [[PubMed](#)]
37. Kim, J.S.; Yoon, J.W.; Hong, Y.J.; Kang, Y.C.; Abdel-Hady, F.; Wazzan, A.A.; Lee, J.H. Highly Sensitive and Selective Detection of Ppb-Level NO₂ Using Multi-Shelled WO₃ Yolk-Shell Spheres. *Sens. Actuators B Chem.* **2016**, *229*, 561–569. [[CrossRef](#)]
38. Natkaeo, A.; Phokharatkul, D.; Hodak, J.H.; Wisitsoraat, A.; Hodak, S.K. Highly Selective Sub-10 ppm H₂S Gas Sensors Based on Ag-Doped CaCu₃Ti₄O₁₂ Films. *Sens. Actuators B Chem.* **2018**, *260*, 571–580. [[CrossRef](#)]
39. Pan, W.; Zhang, Y.; Zhang, D. Self-Assembly Fabrication of Titanium Dioxide Nanospheres-Decorated Tungsten Diselenide Hexagonal Nanosheets for Ethanol Gas Sensing Application. *Appl. Surf. Sci.* **2020**, *527*, 146781. [[CrossRef](#)]
40. Simonenko, T.L.; Simonenko, N.P.; Gorobtsov, P.Y.; Mokrushin, A.S.; Solovey, V.R.; Pozharnitskaya, V.M.; Simonenko, E.P.; Glumov, O.V.; Melnikova, N.A.; Lizunova, A.A.; et al. Pen Plotter Printing of Co₃O₄ Thin Films: Features of the Microstructure, Optical, Electrophysical and Gas-Sensing Properties. *J. Alloys Compd.* **2020**, *832*, 154957. [[CrossRef](#)]
41. Mokrushin, A.S.; Fisenko, N.A.; Gorobtsov, P.Y.; Simonenko, T.L.; Simonenko, E.P.; Simonenko, N.P.; Glumov, O.V.; Melnikova, N.A.; Bukunov, K.A.; Sevastyanov, V.G.; et al. Pen Plotter Printing of ITO Thin Film as a Highly CO Sensitive Component of a Resistive Gas Sensor. *Talanta* **2021**, *221*, 121455. [[CrossRef](#)]
42. Mokrushin, A.S.; Simonenko, T.L.; Simonenko, N.P.; Yu, P.; Kadyrov, N.C.; Simonenko, E.P.; Sevastyanov, V.G.; Kuznetsov, N.T. Chemoresistive Gas-Sensing Properties of Highly Dispersed Nb₂O₅ Obtained by Programmable Precipitation. *J. Alloys Compd.* **2021**, *868*, 159090. [[CrossRef](#)]
43. Nagornov, I.A.; Mokrushin, A.S.; Simonenko, E.P.; Simonenko, N.P.; Gorobtsov, P.Y.; Sevastyanov, V.G.; Kuznetsov, N.T. Zinc Oxide Obtained by the Solvothermal Method with High Sensitivity and Selectivity to Nitrogen Dioxide. *Ceram. Int.* **2020**, *46*, 7756–7766. [[CrossRef](#)]
44. Vallejos, S.; Pizúrová, N.; Gràcia, I.; Sotelo-Vazquez, C.; Čechal, J.; Blackman, C.; Parkin, I.; Cané, C. ZnO Rods with Exposed {100} Facets Grown via a Self-Catalyzed Vapor-Solid Mechanism and Their Photocatalytic and Gas Sensing Properties. *ACS Appl. Mater. Interfaces* **2016**, *8*, 33335–33342. [[CrossRef](#)] [[PubMed](#)]
45. Roy, A.; Sood, A.K. Phonons and Fractons in Sol-Gel Alumina: Raman Study. *Pramana J. Phys.* **1995**, *44*, 201–209. [[CrossRef](#)]
46. Šćepanović, M.; Grujić-Brojčin, M.; Vojisavljević, K.; Bernikc, S.; Srečković, T. Raman Study of Structural Disorder in ZnO Nanopowders. *J. Raman Spectrosc.* **2010**, *41*, 914–921. [[CrossRef](#)]
47. Wu, H.; Wu, G.; Wang, L. Peculiar Porous α -Fe₂O₃, γ -Fe₂O₃ and Fe₃O₄ Nanospheres: Facile Synthesis and Electromagnetic Properties. *Powder Technol.* **2015**, *269*, 443–451. [[CrossRef](#)]
48. Saaedi, A.; Yousefi, R.; Jamali-Sheini, F.; Zak, A.K.; Cheraghizade, M.; Mahmoudian, M.R.; Baghchesara, M.A.; Dezaki, A.S. XPS Studies and Photocurrent Applications of Alkali-Metals-Doped ZnO Nanoparticles under Visible Illumination Conditions. *Phys. E Low-Dimensional Syst. Nanostructures* **2016**, *79*, 113–118. [[CrossRef](#)]
49. Mahana, A.; Mehta, S.K. Potential of Scenedesmus-Fabricated ZnO Nanorods in Photocatalytic Reduction of Methylene Blue under Direct Sunlight: Kinetics and Mechanism. *Environ. Sci. Pollut. Res.* **2021**, *28*, 28234–28250. [[CrossRef](#)]
50. Zhang, Z.; Lu, J.; Yun, T.; Zheng, M.; Pan, J.; Sow, C.H.; Tok, E.S. Desorption of Ambient Gas Molecules and Phase Transformation of α -Fe₂O₃ Nanostructures during Ultrahigh Vacuum Annealing. *J. Phys. Chem. C* **2013**, *117*, 1509–1517. [[CrossRef](#)]
51. Hawn, D.D.; DeKoven, B.M. Deconvolution as a Correction for Photoelectron Inelastic Energy Losses in the Core Level XPS Spectra of Iron Oxides. *Surf. Interface Anal.* **1987**, *10*, 63–74. [[CrossRef](#)]
52. Hu, X.; Yu, J.C.; Gong, J.; Li, Q.; Li, G. α -Fe₂O₃ Nanorings Prepared by a Microwave-Assisted Hydrothermal Process and Their Sensing Properties. *Adv. Mater.* **2007**, *19*, 2324–2329. [[CrossRef](#)]
53. Wang, J.; Wang, Z.; Huang, B.; Ma, Y.; Liu, Y.; Qin, X.; Zhang, X.; Dai, Y. Oxygen Vacancy Induced Band-Gap Narrowing and Enhanced Visible Light Photocatalytic Activity of ZnO. *ACS Appl. Mater. Interfaces* **2012**, *4*, 4024–4030. [[CrossRef](#)] [[PubMed](#)]
54. Ansari, S.A.; Khan, M.M.; Kalathil, S.; Nisar, A.; Lee, J.; Cho, M.H. Oxygen Vacancy Induced Band Gap Narrowing of ZnO Nanostructures by an Electrochemically Active Biofilm. *Nanoscale* **2013**, *5*, 9238–9246. [[CrossRef](#)]
55. Caglar, M.; Ilican, S.; Caglar, Y. Influence of Dopant Concentration on the Optical Properties of ZnO: In Films by Sol-Gel Method. *Thin Solid Films* **2009**, *517*, 5023–5028. [[CrossRef](#)]
56. Gosdy, W.; Orville Thomas, W.J. Electronegativities of the Elements. *J. Chem. Phys.* **1956**, *24*, 439–444. [[CrossRef](#)]
57. Firooz, A.A.; Abbas, A.; Khodadadi, A.A. The Effect of Different Fe₂O₃/ZnO Nanocomposites on Optical Properties. In Proceedings of the 4th International Conference on Nanostructures (ICNS4), Kish Island, Iran, 12–14 March 2012; pp. 10–12. [[CrossRef](#)]
58. Mokrushin, A.S.; Nagornov, I.A.; Simonenko, T.L.; Simonenko, N.P.; Gorobtsov, P.Y.; Khamova, T.V.; Kopitsa, G.P.; Evzrezov, A.N.; Simonenko, E.P.; Sevastyanov, V.G.; et al. Chemoresistive Gas-Sensitive ZnO/Pt Nanocomposites Films Applied by Microplotter Printing with Increased Sensitivity to Benzene and Hydrogen. *Mater. Sci. Eng. B Solid-State Mater. Adv. Technol.* **2021**, *271*, 115233. [[CrossRef](#)]
59. Mokrushin, A.S.; Nagornov, I.A.; Simonenko, T.L.; Simonenko, N.P.; Gorobtsov, P.Y.; Arkhipushkin, I.A.; Simonenko, E.P.; Sevastyanov, V.G.; Kuznetsov, N.T. Gas-Sensitive Nanostructured ZnO Films Praseodymium and Europium Doped: Electrical Conductivity, Selectivity, Influence of UV Irradiation and Humidity. *Appl. Surf. Sci.* **2022**, *589*, 152974. [[CrossRef](#)]

60. NOISH Documentation for Immediately Dangerous to Life or Health Concentrations (IDLHs)-7783064; National Institute Occupational Safety Health: Washington, DC, USA, 1996. Available online: <http://www.cdc.gov/niosh/idlh/7783064.html> (accessed on 14 December 2022).
61. Jung, H.; Cho, W.; Yoo, R.; Lee, H.S.; Choe, Y.S.; Jeon, J.Y.; Lee, W. Highly Selective Real-Time Detection of Breathacetone by Using ZnO Quantum Dots with a Miniaturized Gas Chromatographic Column. *Sens. Actuators B Chem.* **2018**, *274*, 527–532. [[CrossRef](#)]
62. Kim, H.J.; Lee, J.H.; Hyo-Joong, K.; Jong-Heun, L. Highly Sensitive and Selective Gas Sensors Using P-Type Oxide Semiconductors: Overview. *Sens. Actuators B Chem.* **2014**, *192*, 607–627. [[CrossRef](#)]
63. Chen, M.; Wang, Z.; Han, D.; Gu, F.; Guo, G. Porous ZnO Polygonal Nanoflakes: Synthesis, Use in High-Sensitivity NO₂ Gas Sensor, and Proposed Mechanism of Gas Sensing. *J. Phys. Chem. C* **2011**, *115*, 12763–12773. [[CrossRef](#)]
64. Chizhov, A.; Romyantseva, M.; Gaskov, A. Light Activation of Nanocrystalline Metal Oxides for Gas Sensing: Principles, Achievements, Challenges. *Nanomaterials* **2021**, *11*, 892. [[CrossRef](#)] [[PubMed](#)]
65. Zhang, T.; Hui, Y.; Chen, L.; Li, G.; Mao, B.; Zhao, Y. Interfacial Crosslinked Quasi-2D Perovskite with Boosted Carrier Transport and Enhanced Stability. *J. Phys. D. Appl. Phys.* **2018**, *51*, 404001. [[CrossRef](#)]
66. Hong, H.S.; Phan, D.T.; Chung, G.S. High-Sensitivity Humidity Sensors with ZnO Nanorods Based Two-Port Surface Acoustic Wave Delay Line. *Sens. Actuators B Chem.* **2012**, *171–172*, 1283–1287. [[CrossRef](#)]
67. Liang, Y.C.; Hsu, Y.W. Enhanced Sensing Ability of Brush-like Fe₂O₃-ZnO Nanostructures towards NO₂ Gas via Manipulating Material Synergistic Effect. *Int. J. Mol. Sci.* **2021**, *22*, 6884. [[CrossRef](#)]
68. Zhang, B.; Huang, Y.; Vinluan, R.; Wang, S.; Cui, C.; Lu, X.; Peng, C.; Zhang, M.; Zheng, J.; Gao, P.X. Enhancing ZnO Nanowire Gas Sensors Using Au/Fe₂O₃ Hybrid Nanoparticle Decoration. *Nanotechnology* **2020**, *31*, 325505. [[CrossRef](#)] [[PubMed](#)]
69. Wen, Z.; Ren, H.; Li, D.; Lu, X.; Joo, S.W.; Huang, J. A Highly Efficient Acetone Gas Sensor Based on 2D Porous ZnFe₂O₄ Nanosheets. *Sens. Actuators B Chem.* **2023**, *379*, 133287. [[CrossRef](#)]
70. Yang, J.H.; Yuan, K.P.; Zhu, L.Y.; Hang, C.Z.; Li, X.X.; Tao, J.J.; Ma, H.P.; Jiang, A.Q.; Lu, H.L. Facile Synthesis of α -Fe₂O₃/ZnO Core-Shell Nanowires for Enhanced H₂S Sensing. *Sens. Actuators B Chem.* **2020**, *307*, 127617. [[CrossRef](#)]
71. Aleksanyan, M.; Sayunts, A.; Shahkhatuni, G.; Simonyan, Z.; Kasparyan, H.; Kopecký, D. Room Temperature Detection of Hydrogen Peroxide Vapor by Fe₂O₃:ZnO Nanograins. *Nanomaterials* **2022**, *13*, 120. [[CrossRef](#)]
72. Aleksanyan, M.S.; Sayunts, A.G.; Shahkhatuni, G.H.; Aroutiounian, V.M.; Shahnazaryan, G.E. Study of Characteristics of the Sensor Detecting of Low Concentration of Ammonia. *J. Contemp. Phys.* **2021**, *56*, 352–358. [[CrossRef](#)]
73. Aleksanyan, M.S.; Sayunts, A.G.; Shahkhatuni, G.H.; Simonyan, Z.G.; Shahnazaryan, G.E.; Aroutiounian, V.M. Use of Nanostructured Fe₂O₃:ZnO Film for Detection of Hydrogen. *J. Contemp. Phys.* **2022**, *57*, 140–145. [[CrossRef](#)]

Disclaimer/Publisher’s Note: The statements, opinions and data contained in all publications are solely those of the individual author(s) and contributor(s) and not of MDPI and/or the editor(s). MDPI and/or the editor(s) disclaim responsibility for any injury to people or property resulting from any ideas, methods, instructions or products referred to in the content.